Material Parameters and Perspectives for Efficiency Improvements in Perovskite Solar Cells Obtained by Analytical Modeling

Kurt Taretto, Marcos Soldera, and Alejandro Koffman-Frischknecht

***Abstract*—Current perovskite solar cells reach high efficiencies with inexpensive materials and preparation methods. However, in order to understand the current values and obtain even higher efficiencies, the fundamental loss mechanisms of perovskite solar cells must be elucidated and predicted by appropriate models. Here, we adapt an analytical, drift-diffusion model for p-i-n solar cells and obtain accurate fits to measured current–voltage characteristics of planar hysteresis-free perovskite solar cells, covering a range of illumination intensities and perovskite thicknesses. Our results give values of carrier recombination lifetimes above 1 μs, low effective recombination velocities at the interfaces between the perovskite layer and the surrounding layers around 1000 cm/s, built-in voltages that are slightly below the open-circuit voltages of around 1.05 V, and carrier mobilities around 0.1 cm^2/Vs. The obtained parameters indicate that interface and bulk recombination are competing mechanisms, none of which can be ruled out in the case of the studied cells. Furthermore, we find that increasing the built-in voltage can significantly improve efficiency in p-i-n cells, while the implied relatively long diffusion length encourages the investigation of pn-type structures as ideal perovskite solar cell junctions.**

***Index Terms*—Analytical models, efficiency improvements, perovskites, pin solar cells.**

I. Introduction

THE spectacular rise of perovskite solar cells among the scientific community is based on the realization of their great potential to constitute an efficient, low energy impact, mass deployable thin-film photovoltaic technology [1]. Although the current record efficiencies surpass 20% on the laboratory scale [2], even higher efficiencies may be attainable if the main bottlenecks of fundamental loss mechanisms in current devices are identified [3], [4]. A fundamental approach to identify such bottlenecks is explaining the current-density (*J*)/voltage (*V*) characteristics of a solar cell in terms of physical models, which include fundamental material and interface properties. In many cases, an important hurdle in modeling perovskite solar cells is the presence of hysteresis either between forward or backward scans of the *J* versus *V* curve [5], [6]. The physical origin and, hence, the possibility to model this behavior properly, has been debated since the very appearance of perovskite solar cells [7], [8]. In the meantime, several research groups encountered ways to obtain highly efficient hysteresis-free solar cells [5], [9]–[11], paving the way to reliable characterization and certification of device performance.

Here, we apply an analytical model for p-i-n solar cells by treating the perovskite layer as an effective medium with transport and recombination parameters that effectively take into account the individual parameters for electrons and holes [3]. The model is tested by fitting experimental *J(V)* curves of state-of-the art, hysteresis-free lead-halide solar cells. The fits yield mainly four physical parameters: effective carrier lifetime, effective mobility, built-in voltage, and interface recombination velocities at the perovskite-contact layer interfaces.

The next section introduces the *J(V)* equation together with the main physical assumptions, discussing the applicability to the particular case of hysteresis-free perovskite solar cells. We then show the fits to experimental current/voltage curves, contrasting the obtained fit parameters with literature values, and finally suggest possible optimization routes for efficiency improvements.

II. Model and Fitting Strategy

A. Preliminary Observations and Model Assumptions

Although there is an ongoing debate about the shape of the energy band diagram for lead-halide perovskite solar cells, consensus is building up about the perovskite layer being intrinsic, stacked between two conductive layers. Detailed analyses of the recombination nature in the perovskite also point to intrinsic-like behavior [12]. This leads to the possibility that perovskite solar cells may be modeled by either p-i-n or metal-intrinsic-metal junctions [13]. The model for the *J(V)* curve applied here is an analytical drift-diffusion model for p-i-n solar cells, which was previously applied to current/voltage fitting of thin silicon solar cells, as well as organic solar cells [14], [15]. Since the model assumes negligible photovoltaic contribution of the doped layers, only the intrinsic layer (i-layer) is considered as the photoactive material. The electric field is modeled taking into account the built-in voltage $V_{\rm bi}$ given either by the work function and/or doping of the layers on each side of the i-layer. An important feature of the model is that it takes the potential drop at the edges of the i-layer into account, which leaves an equilibrium potential difference of $V_0 < V_{\rm bi}$ in the i-layer. This refinement leads to the equilibrium electric field V_0/d, instead of $V_{\rm bi}/d$, as in previous models, where *d* is the thickness of the

Manuscript received June 28, 2016; revised November 4, 2016; accepted November 6, 2016. Date of publication November 28, 2016; date of current version December 20, 2016. This work was supported by the Agencia Nacional de Promoción Científica y Tecnológica, Argentina, under Project 1401-2011.

The authors are with the PROBIEN–Departamento de Electrotecnia, CONICET–Universidad Nacional del Comahue, Neuquén 8300, Argentina (e-mail: kurt.taretto@fain.uncoma.edu.ar; marcos.soldera@fain.uncoma.edu.ar; alejandrokoffmanf@gmail.com).

Color versions of one or more of the figures in this paper are available online at http://ieeexplore.ieee.org.

Digital Object Identifier 10.1109/JPHOTOV.2016.2627398

i-layer. In the case of thin-film silicon solar cells and organic solar cells, this correction turns out to be a major correction to the conventional constant field approximation, where the potential drop at the interfaces is neglected. Analogously, as shown below, the distinction between V_0 and $V_{\rm bi}$ in lead-halide perovskite solar cells allows recognizing that the electric field in the i-layer vanishes around maximum power conditions, suggesting an optimization route through the choice of contact layers. V_0 is the potential drop within the i-layer, which is given by

$$V_0 = V_{\rm bi} - 4V_t - 2V_t W\left(\frac{1}{2}\left(\frac{V_t d}{V_{\rm bi} L_i}\right)^2 e^{\frac{V_{\rm bi}}{2V_t}}\right) \qquad (1)$$

where the symbol *W* represents the Lambert-W function. Here, V_t is the thermal voltage given by *kT/q*, *k* being Boltzmann's constant; *T* is the absolute temperature; and *q* is the elemental charge. L_i is the dielectric Debye-Hückel length of the intrinsic semiconductor given by $L_i = \sqrt{\varepsilon_r \varepsilon_0 V_t/(2qn_i)}$, with $\varepsilon_r = 6.5$ the lead-halide perovskite relative dielectric constant [16] and ε_0 is the permittivity of vacuum, whereas n_i is the intrinsic carrier concentration. Notice that (1) is valid for $V_{\rm bi} \gg V_t$ and $d \ll L_i$, conditions that are easily fulfilled in thin perovskite cells, where $L_i \approx 1$ cm because of the low intrinsic carrier concentration (see below).

Turning back to the *J(V)* equation, the main assumptions imposed by the model are as follows [14]:

1) low injection conditions;
2) linear recombination rate using a lifetime model;
3) constant, i.e., position independent electron-hole pair photogeneration rate *G*;
4) symmetric cell, i.e., identical free carrier recombination lifetime τ, mobility μ, and effective interface recombination velocity at contacts *S*.

Let us discuss the validity of assumptions 1–4 in some detail for the specific case of $CH_3NH_3PbI_3$ perovskite solar cells. Within the context of the model, assuming low injection conditions imply that upon injection, the electric field in the i-layer is dictated by energy levels and carrier concentrations of the contact layers [14]. This implies that up to the irradiation levels corresponding to standard illumination conditions, the difference between the Fermi level and the highest occupied molecular orbital/lowest unoccupied molecular orbital of the hole/electron transport layers, respectively, remains unchanged. In the case of the modeled perovskite cells, this assumption is justified by the fact that both the PCDTBT (hole transport layer) and the $PC_{60}BM$ (electron transport layer) do not absorb light significantly. According to our optical simulations, the absorbance under AM1.5 100 mW/cm^2 illumination of these thin layers is below 10^{-2} (two orders below the absorbance in the perovskite) along the whole spectrum.

Linear recombination (assumption 2) requires a linearly dependent recombination rate of the excess minority carrier concentrations. Despite several recombination mechanisms acting simultaneously, such linearity has been recently found in the farthest delay time of photoluminescence decay curves of $CH_3NH_3PbI_3$ perovskite films, pointing to defect recombination as the dominating recombination mechanism [17]. Constant photogeneration (assumption 3) is a less-stringent requirement for the evaluation of *J(V)* curves; however, let us show that typical perovskite cells subject to standard spectra illumination have photogeneration rates that do not vary too strongly with depth. Fig. 1 shows the profiles of photogeneration rate *G* as a function of the relative depth to thickness ratio *x/d*, simulated on typical glass/ITO(80 nm)/PEDOT:PSS(15)/PCDTBT(5)/$CH_3NH_3PbI_3$ (*d*)/$PC_{60}BM$(10)/Ag(100) structures. The profiles were obtained using standard transfer-matrix formalisms [18], [19] for coherent layers with a thick superstrate under standard AM1.5G spectrum in the wavelength range from 300 to 800 nm, using the refractive indexes reported in [20]. In the selected range of perovskite thickness from 100 to 400 nm, we see that *G(x)* decreases with fluctuations toward the end of the layer, spreading photogeneration throughout the entire layer thickness. Additionally, detailed comparisons with numerical simulations indicate that in cells with moderately to very efficient carrier collection, constant photogeneration shows no appreciable effect on the current/voltage characteristics compared with solar spectrum illumination. The value of *G* in such comparisons is given by the spatial mean value of the generation profile resulting from a standard spectrum illumination [14]. In conclusion, we assume that the constant photogeneration rate *G* is valid to model current/voltage curves of $CH_3NH_3PbI_3$ cells illuminated under standard conditions.

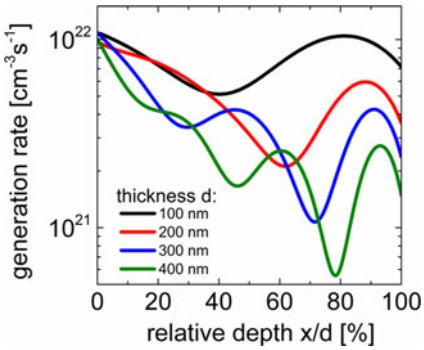

Fig. 1. Free carrier photogeneration rate *G(x)* as a function of perovskite depth in a perovskite solar cell stack composed of glass/ITO(80 nm)/PEDOT:PSS(15)/PCDTBT(5)/CH3NH3PbI3(*d*)/PC60BM(10)/Ag(100). With different perovskite thicknesses *d*, the *G(x)* profiles show fluctuations rather than strongly decaying profiles.

The remaining assumptions pertaining to the symmetric cell approach (assumption 4) require identical recombination lifetime and carrier mobility for electrons and holes. The current understanding of mobilities in lead-halide perovskite films points to similar electron and hole mobilities [21], despite the fact that the measured values are spread by several order of magnitudes, depending on preparation and mobility characterization techniques [4], [22], [23]. In addition, mobility-lifetime products are similar for holes and electrons [23], which imply comparable carrier lifetimes. Moreover, it is worth noting that even if carrier mobilities and lifetimes of electrons and holes are not identical, it was shown that the model is able to fit *J(V)* curves if mobility and lifetime are understood as effective parameters, provided the difference between electron and hole parameters

are within the same order of magnitude [14]. Thus, the effective mobility of electrons and holes corresponds to the ambipolar mobility [24].

B. Current–Voltage Equation

The use of the assumptions described above allows for an analytical solution of the drift-diffusion equations for carriers in the i-layer, which yields the current/voltage curve given by [14]

$$J(V) = J_{\rm dark}(V) - J_{\rm photo}(V) \tag{2}$$

where $J_{\rm photo}$ is the photocurrent density given by the product of maximum attainable photocurrent *qdG* and a voltage-dependent global collection efficiency F_C

$$J_{\rm photo}(V) = qdGF_C(V) \tag{3}$$

with

$$F_C(V) = 2\left(\frac{L}{d}\right)^2 \times \left\{(\beta_1+\beta_2)\,\frac{1+\left(\frac{\beta_1-\beta_2-Sd/D}{\beta_2+Sd/D}\right)e^{-\beta_1/2}}{1+\left(\frac{\beta_1-Sd/D}{\beta_2+Sd/D}\right)e^{-\frac{\beta_1+\beta_2}{2}}} - \beta_1\right\}. \tag{4}$$

Here, β_1 and β_2 are dimensionless parameters given by

$$\beta_{1,2} = \sqrt{\left(\frac{d}{L}\right)^2 + \left(\frac{V-V_0}{2V_t}\right)^2} \pm \left(\frac{V-V_0}{2V_t}\right) \tag{5}$$

where the $\pm$ sign refers to β_1 and β_2, respectively. The effective diffusion constant *D* is obtained from the effective mobility μ from Einstein's relation $D = V_t\mu$, and the effective diffusion length is given by $L = \sqrt{D\tau}$. As seen from the above equations, the photocurrent depends on voltage through the voltage dependence of β_1 and β_2. Depending on the specific material parameters, at sufficiently low bias, (4) correctly yields $F_C = 1$, whereas (3) gives as result the maximum photocurrent $J_{\rm photo}^{\rm max} = qdG$.

The dark current density is given by

$$J_{\rm dark}(V) = J_0(V) \times (e^{\frac{V}{2V_t}} - 1) \tag{6}$$

where J_0 is a voltage-dependent inverse saturation current density given by

$$J_0(V) = \frac{2qn_iD}{d} \times \left(\beta_1 + \frac{\beta_1+\beta_2}{\left(\frac{Sd/D+\beta_2}{Sd/D-\beta_1}\right)e^{\frac{\beta_1+\beta_2}{2}} - 1}\right). \tag{7}$$

Let us briefly highlight the difference between this model and the ideal one-diode model, where $J(V) = J_0(\exp(V/n_{\rm id}V_t) - 1) - J_{\rm photo}$. The one-diode model includes an empirical ideality factor $n_{\rm id}$, while in the present model, the dark current does not rely on any empirical ideality factor, since the exponential term $\exp(V/2V_t)$ fixes the ideality to $n_{\rm id} = 2$, which is traced back to the conditions of linear recombination rate and symmetric cell. Depending on the material parameters, however, the voltage-dependent terms contained in J_0 increase the slope of $J_{\rm dark}$, which can be interpreted as an effective and voltage-dependent ideality. It can be shown that the effective ideality is thus constrained between the values $n_{\rm id} = 1$ and 2, each extreme corresponding to the high and low mobility lifetime product regime, respectively [14].

Following the one-diode model, for a given *J(V)* curve, the effective (or apparent) ideality is obtained by evaluating

$$n_{\rm id} = \left(V_t\frac{d}{dV}(\ln J)\right)^{-1} \tag{8}$$

which is valid for at least $V > 3n_{\rm id}V_t$.

Several parameters involved in the equations above are either known or calculated from material data before fitting. Using the effective density of states masses given in [25] and [26], we obtain [24, eq. (28)] the intrinsic carrier concentration $n_i = 6 \times 10^4$ cm^{-3} at temperature $T = 293$ K and assuming a bandgap $E_g = 1.58$ eV [9]. It can be seen that this remarkably low value of n_i (compared with intrinsic semiconductors of similar bandgap) stems from the combination of low values of both, the effective density of state masses in the valence and in the conduction band of $CH_3NH_3PbI_3$, which range in the order of 0.15–0.23 times the free electron mass [25], [26].

C. Fitting Strategy

The model fits include the effect of series and shunt (or parallel) resistance with area-specific values R_S and R_P, respectively. This leads to the implicit fit equation of the current/voltage curve $J_{\rm fit}(V_{\rm exp})$

$$J_{\rm fit}(V_{\rm exp}) = J(V_{\rm exp} - J_{\rm exp}R_S) + \frac{V_{\rm exp} - J_{\rm exp}R_S}{R_P} \tag{9}$$

where $V_{\rm exp}$ and $J_{\rm exp}$ are the measured values, and *J* obeys (2)–(7). The fitting algorithm uses a simulated annealing minimization strategy, which yielded mean relative fit errors below 6% in all fitted curves.

The fitting strategy consists in obtaining *a priori* three parameters: R_S, R_P, and the photogeneration rate *G,* as shown below, thus leaving only four parameters as fit parameters: built-in voltage $V_{\rm bi}$, effective mobility μ, effective interface recombination velocity *S,* and effective recombination lifetime τ. Regarding the values of the resistances, notice that *dV/dJ* must tend asymptotically to R_P when $V \to -\infty$ and to R_S when $V \to +\infty$, regardless of the characteristics of the solar cell under analysis [27]. Thus, it is possible to obtain R_S by linear fitting the data plotted as *dV/dJ* versus J^{-1}. Notice that this and other similar basic techniques to extract R_S may not work under illumination because the photocurrent is *a priori* unknown at voltages where the effect of R_S is noticeable. The shunt (or parallel) resistance is extracted using $R_P = (dV/dJ)$ from the illuminated curve, under reverse bias [28]. This assumes that the dependence of photocurrent on voltage becomes negligible at low bias voltage (i.e., $dJ_{\rm photo}/dV \to 0$), which holds for efficient cells. This also means that the photocurrent depends significantly on voltage only well above $V \gg V_t$, i.e., $F_C \to 1$ at short circuit and reverse bias. In this case, the effective photogeneration *G* can

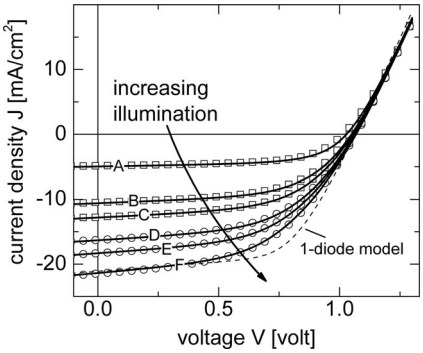

Fig. 2. Illuminated current/voltage curves of a solar cell with 300 nm perovskite thickness (data symbols), under illumination intensities increasing in the direction of the arrow, and fitted by the model (solid lines). See text for fitting parameter values. The dashed line is obtained with a one-diode model corresponding to curve F.

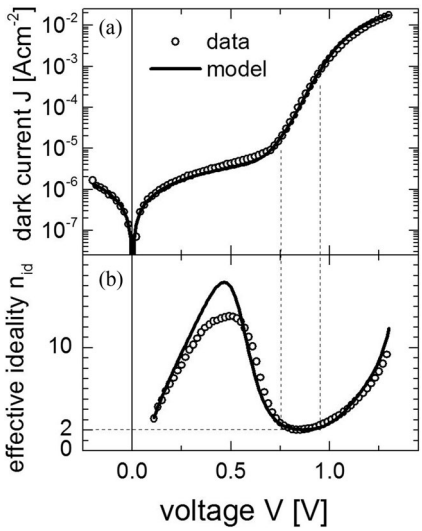

Fig. 3. Plot (a) shows the dark *J(V)* curve in logaritmic scale, showing good agreement between data (open symbols) and model fit (solid line). Plot (b) shows the voltage-dependent effective ideality obtained by applying (8) of the main text to the curves in plot (a).

be approximated by

$$G \cong |J_{\rm SC}| / qd. \tag{10}$$

In the next section, we show that this approximation is valid in all the cells studied here.

III. Results and Discussions

We analyze current/voltage curves and the obtained model fits for two series of data: a light intensity series on a given cell and a series of cells with varying $CH_3NH_3PbI_3$ thickness. The cells are prepared by sequential deposition of ITO-coated glass [9], according to the layer stack glass/ITO(80 nm)/PEDOT:PSS(15)/PCDTBT(5)/$CH_3NH_3PbI_3$ *(thickness d)*/PC60BM(10)/Ag(100). In all the cells studied here, the perovskite $CH_3NH_3PbI_3$ is deposited by coevaporation, the organic layers are prepared by spin coating and the silver layer by vacuum thermal evaporation [9, supplementary information].

Starting with the illumination series, Fig. 2 shows the current/voltage curves (data symbols) of a solar cell with 300 nm perovskite thickness, under illumination intensities increasing from curve A to F in the direction of the arrow. At full standard illumination, this cell delivers the following output parameters: open-circuit voltage $V_{\rm OC} = 1.07$ V, short-circuit current density $J_{\rm SC} = 21.5$ mAcm^{-2}, fill-factor FF $= 49.9\%$, and efficiency $\eta = 11.4\%$. The solid lines in Fig. 2 are model fits, showing very good agreement to the data, collectively showing less than 5.2% overall mean error. The fit to the 100% illuminated curve (F) yields the effective lifetime $\tau = 1.31\mu$s, effective mobility $\mu = 0.031$ cm^2/Vs, effective interface recombination velocity $S = 62$ cm/s (which translates into 460 cm/s at the actual interface, see below), and built-in voltage $V_{\rm bi} = 0.951$ V, which implies $V_0 = 0.849$ V according to (1). The obtained effective generation rate obtained with the criterion given by (10) is $G = 3.96 \times 10^{21}$ cm^{-3}s^{-1}, a value only 1% smaller than the calculated mean generation rate (obtained from Fig. 1 at 300 nm thickness). Further, the *dV/dJ* analysis to curve F previous to the fit yields a specific series resistance $R_S = 10.5\ \Omega$ cm^2 and parallel resistance $R_P = 0.425$ kΩ cm^2, as described previously. The simulated *J(V)* curves with smaller illumination intensities (solid lines on data A-E in Fig. 2) use the same set of parameters, except for R_P, which is obtained individually for each case (see Fig. 5 and discussion below) and, of course, except for *G*, which depends on illumination.

In order to compare to the p-i-n model, Fig. 2 includes a nonideal one-diode model curve (dashed line), which uses R_S and R_P values corresponding to curve F: an ideality $n_{\rm id} = 2$ and J_0 obtained from (7) in [29]. The notorious deviation from the experimental curves suggests that the voltage-independent saturation current density and photocurrent of the one-diode model are unacceptable approximations in this case.

Let us discuss the parameter values obtained from the model. The lifetime value just above $\tau = 1\ \mu$s matches the typical photoluminescence decay lifetime measurements in $CH_3NH_3PbI_3$ films obtained by either solution methods [30]–[32] or values around 0.5 μs measured by charge transient time [33], highlighting the exceptionally low recombination in $CH_3NH_3PbI_3$ perovskites. The mobility $\mu = 0.03$ cm^2/Vs obtained from the fit is considerably lower than values around 100 cm^2/Vs reported from Hall measurements on single crystals [21] but approaches the value 0.06 cm^2/Vs obtained by canonical time-of-flight measurements in vapor-deposited $CH_3NH_3PbI_3$ films [23] and surpasses by an order of magnitude the values obtained by other techniques [22], which nevertheless deliver efficient cells. Such discrepancies are apparently explained by the increased impurity concentrations and grain boundaries present in thin films compared with single crystals [34], but may also arise from experimental uncertainties and even the choice of the experimental method itself [22]. Regarding the very low effective interface recombination velocity, let us recall that the parameter *S* in the model is an effective recombination velocity as seen from the i-layer, while the "true" interface recombination velocity $S_{\rm int}$

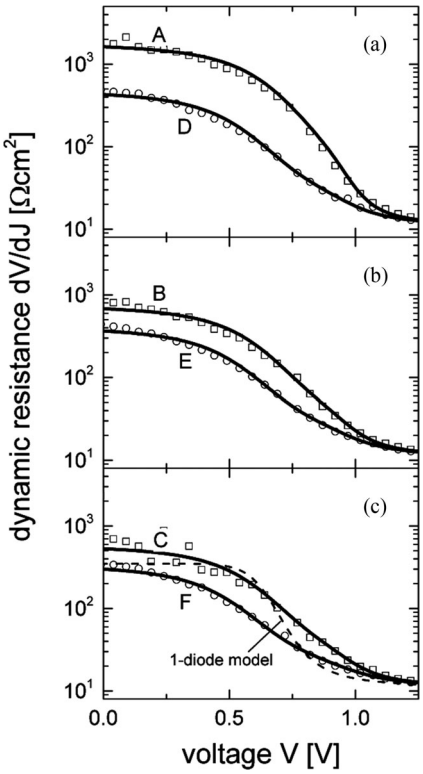

Fig. 4. Specific dynamic resistance corresponding to the *J(V)* curves (symbols) A–F (shown in Fig. 2) and the corresponding *J(V)* fits (solid lines). At the extremes of low and high voltages, these curves tend to the values of parallel resistance and series resistance, respectively. The dashed line in plot (c) is obtained with a one-diode model corresponding to curve F and is affected by the resistance values, showing a much more steep decrease at intermediate voltages than the model curves.

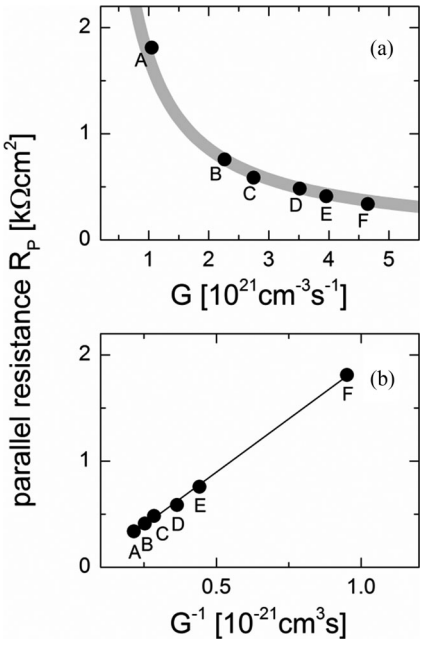

Fig. 5. Specific parallel resistance R_p as a function of effective generation rate *G* (plot a), obtained from curves A–F (Fig. 2). Plotted against the inverse effective generation rate G^{-1} [plot (b)], the values seemingly follow a linear dependence (straight line), possibly pointing to a photoconductivity effect of the organic hole transport layer.

may be considerably larger, depending on the potential drop at the interface. Since the potential drops at the interfaces are taken into account by the difference $V_{\rm bi} - V_0$, within the symmetrical cell model, it is possible to obtain $S_{\rm int}$ by evaluating

$$S_{\rm int} = S \times \exp\left(\frac{V_{\rm bi} - V_0}{2V_t}\right). \tag{11}$$

In the present cell with $V_{\rm bi} = 0.951$ V, $V_0 = 0.849$ V, and $S = 62$ cm/ s, we obtain $S_{\rm int} \cong 460$ cm/s. Such low values have been recently obtained by curve fitting *J(V)* characteristics with analytical models [35], and deduced from photoluminescence measurements [17], as well as in unpassivated, solution grown $CH_3NH_3PbI_3$ single crystals [36]. Notice that in the analytical model proposed by Sun *et al*. [35], bulk recombination was neglected entirely, making interface recombination the dominating recombination mechanism. The combination of high lifetimes and low interface recombination velocity obtained here, however, indicate that it is difficult to rule out *a priori* either recombination mechanism as dominating recombination in the cell throughout the whole *J(V)* curve. By inspection of (4) and (7), a first comparison between the bulk recombination and interface recombination is possible by comparing $\beta_{1,2}$ from (5) and the quantity Sd/D which, taking $V = V_0$ for simplicity, yield $\beta_{1,2} = 0.94$ and $Sd/D = 2.39$, meaning comparable interface and bulk recombination near open circuit. At short circuit ($V = 0$), it turns out that $\beta_2 \gg Sd/D$, making bulk recombination the dominating mechanism.

The fit to the dark current/voltage curve is shown in Fig. 3, where plot (a) shows the logarithmic *J* versus *V* dependence of the data (open circles) and the model fit (solid line), whereas plot (b) shows the effective ideality obtained by applying (8) to both the data and the model. In the fitting procedure, the values of R_S, μ, *S,* and $V_{\rm bi}$ are set equal to the illuminated case, resulting in the free fit parameters $R_{p,\rm dark} = 145$ kΩ cm^2 and $\tau_{\rm dark} = 101$ ns.

In general, as known from the inorganic semiconductors, the occurrence of a much smaller recombination lifetime in the dark as compared with the illuminated case may arise from the injection-dependent carrier trapping by defect states under illumination (see [28], p. 403). The injection level dependence of lifetime in lead-halide perovskites has recently been extensively discussed in [12], where it is seen that lead-halide perovskites may exhibit an increasing τ with light from dark up to excitation levels compatible with nonconcentrating, standard solar irradiation conditions. Moreover, since this effect depends on the nature and concentration of defect levels, we expect that the illumination dependence of τ depends on sample preparation conditions and methods.

It seems useful to further check the quality of the fits by obtaining the dynamic resistance *dV/dJ* corresponding to the curves of Fig. 2. We find that this plot helps revealing two aspects: the accuracy of the shape of the voltage dependence of the photocurrent and the accuracy of the values of R_S and R_P. Fig. 4(a)–(c) shows the dynamic resistance (in Ω cm^2), as a function of voltage, obtained for *J(V)* data A–F from Fig. 2 and the corresponding fit curves (the curves are shown in

different graphs to avoid superposition). First, let us notice that at low voltages, *dV/dJ* tends to the values of R_P obtained at each illumination (cf., Fig. 5 below), whereas at large voltages it tends to the series resistance $R_S = 10.5\ \Omega\text{cm}^2$. For comparison, plot (c) in Fig. 4 includes *dV/dJ* obtained by the one-diode model (dashed line) with resistance effects using the R_S and R_P values corresponding to curve F and an ideality $n_{\text{id}} = 2$, i.e., the same ideality as resulting from the dark curve of Fig. 3(b). As we can see, the one-diode model yields large deviations of *dV/dJ* at intermediate voltages, tending much more rapidly to R_S at the highest voltages, which stems from assuming voltage-independent J_0 and J_{photo}. Using an ideality of 1 yields even worse results (not shown in Figs. 2 and 3). This was also observed in other type of p-i-n solar cells [14], highlighting the importance of voltage-dependent saturation current densities and photocurrents.

Let us turn to the dependence of parallel resistance R_P on illumination corresponding to the fits in Fig. 2. As can be seen in Fig. 5(a), from illumination A–F, R_P decreases monotonously with increasing generation rate. The thick gray line serves as a guide to the eye. The observed decrease appears frequently in perovskite solar cells with organic functional layers [37]. We can trace back the origin of this R_P decrease with the aid of Fig. 5(b), which displays the same data versus the inverse generation rate *G*, revealing a linear trend (straight line).

The linearity of R_P versus G^{-1} shown in Fig. 5(b) was observed previously in current/voltage curves of organic solar cells containing fullerene layers. Detailed analyses of the voltage and illumination dependence of current/voltage and quantum-efficiency measurements showed that photoconductivity originated a linear, voltage-dependent decrease in reverse current. This effect mimics an ohmic shunt path [38] and originates in free carrier photogeneration by the splitting of excitons photogenerated in the fullerene layer by the electric field [39].

Turning to the series of data of cells with increasing perovskite thickness, we proceed to the fits of current/voltage curves having $d = 180$ nm/260 nm/340 nm/370 nm $CH_3NH_3PbI_3$ thickness. These cells show higher efficiency than the previously analyzed case, reaching $\eta = 15.2\%$ with $d = 370$ nm [9, see Table I for further solar cell output data]. Fig. 6(a) and (b) shows the data (circles) and corresponding fits (solid lines) and Table I lists the physical parameters for each case. As we can see from the fits, the model is able to reach an excellent agreement in all cases. The calculated global mean error between fits and data did not surpass 5.4% relative, collectively.

Inspecting the results of Table I, we notice that, independently of thickness, the cells profit from high recombination lifetimes between $\tau = 4$ and 10 μs. The mobilities are all in a narrow range, ranging from $\mu = 0.05$ to $0.11\ \text{cm}^2/\text{Vs}$. The obtained mobilities and lifetimes translate into effective diffusion lengths that range from $L = 411$ nm (with $d = 180$ nm) to $L = 1590$ nm ($d = 370$ nm). Since the diffusion lengths are considerably higher than the layer thickness *d* in every case, it can be concluded that these perovskite cells could profit from a pn instead of a p-i-n junction, provided some doping effect could be possible. The prospect of a pn-type perovskite junction seems promising in the light of recent investigations on controlled self-doping techniques applied to perovskites [40], which were also predicted theoretically [41]. Moreover, the very low interface recombination also strengthens the prospects for efficient pn structures: with *S* between 67.5 and 316 cm/s; the actual interface recombination velocity according to (11) yields $S_{\text{int}} = 1043$–3050 cm/s, ensuring high carrier collection and low recombination at open-circuit conditions.

Except for the lifetimes, we do not find clear correlation of the fit parameters with thickness; the rather narrow ranges of values covered by the fit parameters possibly originate from slight variations of preparation conditions from sample to sample. In the case of the lifetime, however, we observe a steady increase with thickness. A possible explanation for this could be related to the occurrence of larger crystalline grains in thicker samples [42], [43], leading to smaller influence of grain boundary recombination in the thicker cells and, thus, higher effective lifetime.

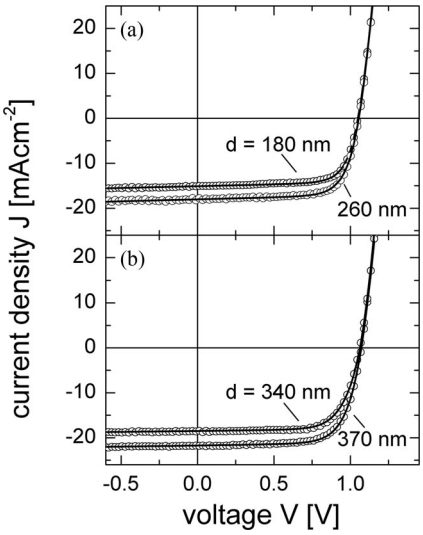

Fig. 6. Current/voltage curves of perovskite solar cells with increasing perovskite thickness (open circles), shown in separate plots to avoid superposition. The model fits (solid lines) accurately follow each of the curves.

TABLE I
MODEL PARAMETERS FOR EACH PEROVSKITE LAYER THICKNESS d: SPECIFIC SERIES AND PARALLEL RESISTANCE R_S, R_P, RESPECTIVELY, EFFECTIVE GENERATION RATE *G*, EXTRACTED BY ANALYZING THE CURVES BEFORE FITTING, AND FOUR FITTING PARAMETERS (BOLD FACE), NAMELY, BUILT-IN VOLTAGE V_{bi}, EFFECTIVE MOBILITY μ, EFFECTIVE LIFETIME τ, AND SURFACE RECOMBINATION VELOCITY *S*. THE LAST TWO ROWS SHOW THE VALUES CALCULATED FOR THE POTENTIAL ACROSS THE I-LAYER V_0 AND THE ACTUAL INTERFACE VELOCITY S_{int}

Model parameters	d = 180 rm	d = 260 rm	d = 340 rm	d = 370 rm
$R_S\ [\Omega\text{cm}^2]$	1.92	1.68	1.33	1.89
$R_P\ [\text{k}\Omega\text{cm}^2]$	1.36	1180	2.72	3.18
$G\ [10^{21}\text{cm}^{-3}\text{s}^{-1}]$	5.25	4.34	3.40	3.67
$\boldsymbol{V_{bi}}\ [V]$	**0.963**	**0.98**	**0.927**	**1.01**
$\boldsymbol{\mu}\ [cm^2/Vs]$	**0.065**	**0.080**	**0.050**	**0.11**
τ **[μs]**	**1.04**	**1.9**	**3.51**	**9.01**
***S* [cm/s]**	**141**	**199**	**67.5**	**316**
$V_0\ [V]$	0.862	0.875	0.826	0.899
S_{int} [cm/s]	1043	1460	501	3050

Analyzing the influence of V_{bi} on the photocurrent, we notice that even sticking to p-i-n junctions may leave room for improvement. Notice that the built-in voltages between 0.93 and 1.01 V are slightly below the open-circuit voltages $V_{\rm OC}$, which are all close to 1.05 V [9, see Table I]. Since in the present cases V_0, the actual potential available for the electric field across the i-layer is about 100 mV (i.e., 10% relative) below $V_{\rm bi}$, it turns out that the photocurrent decays sharply already around the maximum power point voltages $V_{\rm mpp}$. Therefore, according to our results, the studied cells could also profit from enhancing photocarrier collection at maximum power conditions, by strengthening the built-in field. Quantitatively, the model predicts that for the cell with $d = 370$ nm, if we fix all parameters but increase $V_{\rm bi}$ from 200 mV to $V_{\rm bi} = 1.2$ V (cf., Table I, last column), the efficiency increases by 20% relative from 15.2% to 18.3%. Our calculations show that this large impact of $V_{\rm bi}$ on efficiency is directly attained through the improvement of both the maximum power point voltage $V_{\rm mpp}$ and current $J_{\rm mpp}$. This suggests that tweaking the work function at the layers sandwiching the perovskite layer could significantly improve device efficiency.

On a last note, let us mention that a further validation of the model presented here could be possible for instance modeling the temperature dependence of the current–voltage curves. This would enable contrasting fitting parameters with experimental results of temperature dependence of mobility, bandgap, and density of states effective masses. In addition, it seems of relevance for future work to explore the sensitivity of the fits to the relative dielectric constant, in view of recently reported data [44] showing higher dielectric constants than traditionally known.

IV. Conclusion

This contribution applies a physics-based, analytical model for the current/voltage curve of p-i-n solar cells to state of the art $CH_3NH_3PbI_3$-based solar cells sandwiched by organic functional layers. In order to be applicable by the experimentalist to design and predict the behavior of $CH_3NH_3PbI_3$-based solar cells, an important condition to be met in the particular system under study is the linearity of the carrier recombination rate, which can be obtained by different techniques (see, e.g., [17]). Within the group of samples studied here, the model is able to fit accurately the illumination dependent current/voltage curves, as well as $CH_3NH_3PbI_3$ thickness series. The illumination series shows a linear proportionality between parallel (or shunt) resistance with inverse photogeneration rate, suggesting a photoconductivity effect in the PCBM hole transporting layer. Further, the extracted fit parameters are around the following values: built-in voltages of 1 V (i.e., below the open-circuit voltage), effective carrier mobility 0.1 $\rm cm^2/Vs$, lifetimes above 1 μs under illumination, and interface recombination velocities around 1000 cm/s. The combination of these parameters suggests that bulk recombination and interface recombination are competing mechanisms, bulk recombination dominating toward low voltages and interface recombination dominating near open-circuit conditions. The low interface recombination velocities and the high implied diffusion length, which clearly surpasses the perovskite layer thickness, suggest that the efficiency of these cells could improve by adopting a pn homojunction. Additionally, our model predicts that also p-i-n junctions could profit significantly if the built-in voltage is increased beyond the open-circuit voltage.

Acknowledgment

The authors are grateful to Q. Lin (Centre for Organic Photonics and Electronics, University of Queensland, Brisbane, Qld., Australia) for kindly providing the current–voltage measurements of perovskite solar cells and discussion of preliminary results.

References

[1] Q. Lin, A. Armin, P. L. Burn, and P. Meredith, "Organohalide perovskites for solar energy conversion," *Accounts Chem. Res.*, vol. 49, no. 3, pp. 545–553, Mar. 2016.

[2] M. A. Green, K. Emery, Y. Hishikawa, W. Warta, and E. D. Dunlop, "Solar cell efficiency tables (version 47)," *Prog. Photovolt., Res. Appl.*, vol. 24, no. 1, pp. 3–11, Jan. 2016.

[3] T. Kirchartz, J. Bisquert, I. Mora-Sero, and G. Garcia-Belmonte, "Classification of solar cells according to mechanisms of charge separation and charge collection," *Phys. Chem. Chem. Phys.*, vol. 17, no. 6, pp. 4007–4014, 2015.

[4] C. S. Ponseca *et al.*, "Organometal halide perovskite solar cell materials rationalized: Ultrafast charge generation, high and microsecond-long balanced mobilities, and slow recombination," *J. Amer. Chem. Soc.*, vol. 136, no. 14, pp. 5189–5192, Apr. 2014.

[5] N. J. Jeon *et al.*, "Solvent engineering for high-performance inorganic–organic hybrid perovskite solar cells," *Nature Mater.*, vol. 13, no. 9, pp. 897–903, Sep. 2014.

[6] E. L. Unger *et al.*, "Hysteresis and transient behavior in current–voltage measurements of hybrid-perovskite absorber solar cells," *Energy Environ. Sci.*, vol. 7, no. 11, pp. 3690–3698, 2014.

[7] J. Wei *et al.*, "Hysteresis analysis based on the ferroelectric effect in hybrid perovskite solar cells," *J. Phys. Chem. Lett.*, vol. 5, no. 21, pp. 3937–3945, Nov. 2014.

[8] R. S. Sanchez *et al.*, "Slow dynamic processes in lead halide perovskite solar cells. Characteristic times and hysteresis," *J. Phys. Chem. Lett.*, vol. 5, no. 13, pp. 2357–2363, 2014.

[9] Q. Lin, A. Armin, R. C. R. Nagiri, P. L. Burn, and P. Meredith, "Electro-optics of perovskite solar cells," *Nature Photon.*, vol. 9, no. 2, pp. 106–112, Feb. 2015.

[10] Y. Hou *et al.*, "Low-temperature and hysteresis-free electron-transporting layers for efficient, regular, and planar structure perovskite solar cells," *Adv. Energy Mater.*, vol. 5, no. 20, Oct. 2015, Art. no. 1501056.

[11] H. Yoon, S. M. Kang, J.-K. Lee, and M. Choi, "Hysteresis-free low-temperature-processed planar perovskite solar cells with 19.1% efficiency," *Energy Environ. Sci.*, vol. 9, pp. 2262–2266, May 2016.

[12] F. Staub *et al*., "Beyond bulk lifetimes: Insights into lead halide perovskite films from time-resolved photoluminescence," *Phys. Rev. Appl.*, vol. 6, no. 4, Oct. 2016, Art. no. 044017.

[13] A. R. bin Mohd. Yusoff and M. K. Nazeeruddin, "Organohalide lead perovskites for photovoltaic applications," *J. Phys. Chem. Lett.*, vol. 7, no. 5, pp. 851–866, Mar. 2016.

[14] K. Taretto, "New explicit current/voltage equation for p-i-n solar cells including interface potential drops and drift/diffusion transport," *Prog. Photovolt., Res. Appl.*, vol. 22, no. 8, pp. 870–884, 2014.

[15] K. Taretto, A. Koffman-Frischknecht, and M. Soldera, "Light and dark current–voltage fits of bulk heterojunction cells using a new analytical drift-diffusion model," in *Proc. 28th Eur. Photovolt. Sol. Energy Conf. Exhib.*, Paris, France, 2013, pp. 2718–2722.

[16] M. Hirasawa, T. Ishihara, T. Goto, K. Uchida, and N. Miura, "Magnetoabsorption of the lowest exciton in perovskite-type compound $(CH_3NH_3)PbI_3$," *Physica B, Condens. Matter*, vol. 201, pp. 427–430, Jul./Aug. 1994.

[17] F. Staub *et al.*, "Beyond bulk lifetimes: Insights into lead halide perovskite films from time-resolved photoluminescence," *Phys. Rev. Appl.*, vol. 6, 2016, Art. no. 044017.

[18] L. A. A. Pettersson, L. S. Roman, and O. Inganas, "Modeling photocurrent action spectra of photovoltaic devices based on organic thin films," *J. Appl. Phys.*, vol. 86, no. 1, pp. 487–496, Jul. 1999.
[19] G. F. Burkhard, E. T. Hoke, and M. D. McGehee, "Accounting for interference, scattering, and electrode absorption to make accurate internal quantum efficiency measurements in organic and other thin solar cells," *Adv. Mater.*, vol. 22, no. 30, pp. 3293–3297, Aug. 2010.
[20] Y. Jiang, M. A. Green, R. Sheng, and A. Ho-Baillie, "Room temperature optical properties of organic–inorganic lead halide perovskites," *Sol. Energy Mater. Sol. Cells*, vol. 137, pp. 253–257, 2015.
[21] T. M. Brenner *et al.*, "Are mobilities in hybrid organic–inorganic halide perovskites actually 'high'?" *J. Phys. Chem. Lett.*, vol. 6, no. 23, pp. 4754–4757, Dec. 2015.
[22] Y. Chen, J. Peng, D. Su, X. Chen, and Z. Liang, "Efficient and balanced charge transport revealed in planar perovskite solar cells," *ACS Appl. Mater. Interfaces*, vol. 7, no. 8, pp. 4471–4475, Mar. 2015.
[23] B. Maynard *et al.*, "Electron and hole drift mobility measurements on methylammonium lead iodide perovskite solar cells," *Appl. Phys. Lett.*, vol. 108, no. 17, Apr. 2016, Art. no. 173505.
[24] S. M. Sze and K. K. Ng, *Physics of Semiconductor Devices*. Hoboken, NJ, USA: Wiley, 2006.
[25] Y. Zhou, F. Huang, Y.-B. Cheng, and A. Gray-Weale, "Photovoltaic performance and the energy landscape of $CH_3NH_3PbI_3$," *Phys. Chem. Chem. Phys.*, vol. 17, no. 35, pp. 22604–22615, Aug. 2015.
[26] M. R. Filip, C. Verdi, and F. Giustino, "GW band structures and carrier effective masses of $CH_3NH_3PbI_3$ and hypothetical perovskites of the type $APbI_3$: A = NH_4, PH_4, AsH_4, and SbH_4," *J. Phys. Chem. C*, vol. 119, no. 45, pp. 25209–25219, Nov. 2015.
[27] J. H. Werner, "Schottky barrier and pn-junction I/V plots—Small signal evaluation," *Appl. Phys. A*, vol. 47, no. 3, pp. 291–300, Nov. 1988.
[28] D. K. Schroder, *Semiconductor Material and Device Characterization*, 3rd ed. Hoboken, NJ, USA: Wiley-IEEE Press, 2006.
[29] K. Taretto, M. Soldera, and M. Troviano, "Accurate explicit equations for the fill factor of real solar cells—Applications to thin-film solar cells," *Prog. Photovolt., Res. Appl.*, vol. 21, no. 7, pp. 1489–1498, 2013.
[30] H. Zhou *et al.*, "Interface engineering of highly efficient perovskite solar cells," *Science*, vol. 345, no. 6196, pp. 542–546, 2014.
[31] D. W. de Quilettes *et al*., "Impact of microstructure on local carrier lifetime in perovskite solar cells," *Science*, vol. 348, no. 6235, pp. 683–686, 2015.
[32] N. D. Marco *et al*., "Guanidinium: A route to enhanced carrier lifetime and open-circuit voltage in hybrid perovskite solar cells," *Nano Lett.*, vol. 16, no. 2, pp. 1009–1016, 2016.
[33] Y. Shao, Z. Xiao, C. Bi, Y. Yuan, and J. Huang, "Origin and elimination of photocurrent hysteresis by fullerene passivation in $CH_3NH_3PbI_3$ planar heterojunction solar cells," *Nature Commun.*, vol. 5, 2014, Art. no. 5784.
[34] T. M. Brenner, D. A. Egger, L. Kronik, G. Hodes, and D. Cahen, "Hybrid organic–inorganic perovskites: Low-cost semiconductors with intriguing charge-transport properties," *Nature Rev. Mater.*, vol. 1, Jan. 2016, Art. no. 15007.
[35] X. Sun, R. Asadpour, W. Nie, A. D. Mohite, and M. A. Alam, "A physics-based analytical model for perovskite solar cells," *IEEE J. Photovolt.*, vol. 5, no. 5, pp. 1389–1394, Sep. 2015.
[36] Y. Yang *et al*., "Low surface recombination velocity in solution-grown $CH_3NH_3PbBr_3$ perovskite single crystal," *Nature Commun.*, vol. 6, Aug. 2015, Art. no. 7961.
[37] O. Malinkiewicz *et al*., "Perovskite solar cells employing organic charge-transport layers," *Nature Photon.*, vol. 8, no. 2, pp. 128–132, Feb. 2014.
[38] W.-I. Jeong *et al*., "Photoconductivity of C_{60} as an origin of bias-dependent photocurrent in organic photovoltaics," *Adv. Funct. Mater.*, vol. 22, no. 14, pp. 3089–3094, Jul. 2012.
[39] C. K. Renshaw, J. D. Zimmerman, B. E. Lassiter, and S. R. Forrest, "Photoconductivity in donor-acceptor heterojunction organic photovoltaics," *Phys. Rev. B*, vol. 86, no. 8, Aug. 2012, Art. no. 85324.
[40] Q. Wang *et al.*, "Qualifying composition dependent p and n self-doping in $CH_3NH_3PbI_3$," *Appl. Phys. Lett.*, vol. 105, no. 16, Oct. 2014, Art. no. 163508.
[41] J. Kim, S.-H. Lee, J. H. Lee, and K.-H. Hong, "The role of intrinsic defects in methylammonium lead iodide perovskite," *J. Phys. Chem. Lett.*, vol. 5, no. 8, pp. 1312–1317, Apr. 2014.
[42] Q. Chen *et al.*, "Planar heterojunction perovskite solar cells via vapor-assisted solution process," *J. Amer. Chem. Soc.*, vol. 136, no. 2, pp. 622–625, Jan. 2014.
[43] C. V. Thompson, "Structure evolution during processing of polycrystalline films," *Annu. Rev. Mater. Sci.*, vol. 30, no. 1, pp. 159–190, 2000.
[44] M. Sendner *et al.*, "Optical phonons in methylammonium lead halide perovskites and implications for charge transport," *Mater. Horiz.*, vol. 3, no. 6, pp. 613–620, 2016.

Authors' photographs and biographies not available at the time of publication.